

This item is likely protected under Title 17 of the U.S. Copyright Law. Unless on a Creative Commons license, for uses protected by Copyright Law, contact the copyright holder or the author.

Access to this work was provided by the University of Maryland, Baltimore County (UMBC) ScholarWorks@UMBC digital repository on the Maryland Shared Open Access (MD-SOAR) platform.

Please provide feedback

Please support the ScholarWorks@UMBC repository by emailing scholarworks-group@umbc.edu and telling us what having access to this work means to you and why it's important to you. Thank you.

The acceleration of pickup ions at shock waves: Test particle-mesh simulations

A. S. Lipatov,^{1,2} G. P. Zank, and H. L. Pauls

Abstract. A mechanism for the acceleration of pickup ions by repeated reflection from the electrostatic cross-shock potential of a quasi-perpendicular shock was proposed independently by Zank *et al.* [1996b] and Lee *et al.* [1996]. The acceleration mechanism, known variously as Multiply Reflected Ion (MRI) acceleration or “shock surfing,” was studied by these authors in the limit of an idealized shock, which possessed neither fine-scale structure (distinct foot, ramp, or overshoot) nor pickup ion scattering turbulence. Here the acceleration of pickup ions at cometary and interplanetary shocks and at the termination shock is studied in the “test” particle limit on the basis of a particle-mesh simulation. All simulations assume a shell distribution for the pickup ions (either pickup protons or helium), and the dynamics of pickup ions propagating in a fixed electromagnetic field profile are investigated. The effect of a shock foot, ramp and overshoot on the acceleration of pickup ions at perpendicular and oblique shocks is described. The acceleration of pickup ions in the presence of strong turbulence inside the foreshock region is also addressed. For quasi-perpendicular shocks with structure, we obtained the following results. First, the accelerated H^+ and He^+ spectrum is a very hard power law $\propto E^{-k}$, $k = 0.92 - 1.2$, which is much harder than that predicted by diffusive shock acceleration. Also, as θ_{bn} , the angle between the upstream magnetic field and shock normal, decreases from 90° , the accelerated pickup ion spectrum flattens until MRI acceleration ceases. Second, the fine structure of the shock is found to reduce slightly the maximum energy gain for an accelerated pickup ion compared to that gained at an unstructured shock. Third, a flat turbulence spectrum is found to lead to an increase in the maximum energy for transmitted pickup ions, whereas a power law turbulence spectrum leads to a modest reduction in the maximum pickup ion energy gain. However, the basic MRI acceleration mechanism continues to operate in the presence of turbulent magnetic fluctuations and the characteristic hard spectra are preserved. Fourth, MRI acceleration is found to work only for those shocks for which $\theta_{bn} \geq 60^\circ - 70^\circ$. The results from the test particle simulations described here are also used to interpret particle acceleration in self-consistent hybrid simulations.

1. Introduction

The transforming of supersonic flow energy into electromagnetic waves and heated and accelerated particles at collisionless shock fronts is a fundamental dissipative process in space and astrophysical plasma systems. Shock waves are ubiquitous, occurring as bow shocks near planets and comets, as interplanetary shocks, the termination shock (TS) and possibly the bow shock near the heliopause; as shocks generated by solar flares, and as shock waves propagating from astrophysical objects.

However, a detailed plasma physical understanding of how and which particles are extracted from the thermal plasma to be preferentially energized awaits elucidation.

In this paper, we address at a test particle level the acceleration of pickup ions at shocks in the solar wind. To a considerable extent, this work is motivated by the direct observation of accelerated pickup ions by Ulysses at a weak corotating shock [Gloeckler *et al.*, 1994]. Both pickup H^+ and He^+ were observed by the Solar Wind Ion Composition (SWICS) instrument to possess very hard power law spectra which extend directly out of the expected pickup ion distribution [Vasyliunas and Siscoe, 1976] to energies well in excess of the characteristic pickup ion cutoff velocity $v = 2u_{SW}$ (in the spacecraft frame), where v denotes particle velocity and u_{SW} denotes the solar wind flow velocity. It was observed too that $\sim 43\%$ of the pickup protons H^+ and $\sim 16\%$ of the He^+ were accelerated by the shock. The hardness of the pickup ion spectrum was quite inconsistent with the expectations of diffusive, first-order, Fermi shock acceleration. It is generally thought that diffusive shock

¹Also at Department of Problems of Physics and Energetics, Moscow Institute of Physics and Technology, Moscow.

²Now at Dialogue-Science Inc., Computer Center, Russian Academy of Sciences, Moscow.

acceleration should favor the acceleration of heavy ions over lighter ions since the larger gyroradii ions would be “injected” more easily into the acceleration process. That neither expectation is met poses a challenge for models of particle acceleration at shock waves.

Besides diffusive shock acceleration, two alternatives for accelerating pickup ions at weak quasi-perpendicular shocks are shock drift acceleration [Decker, 1983, 1988; Armstrong et al., 1985; Decker and Vlahos, 1986] and Multiply Reflected Ion (MRI) acceleration or shock surfing, proposed originally by Sagdeev [1966], Sagdeev and Shapiro [1973], and Katsouleas and Dawson [1983], and later in the context of pickup ion acceleration by Zank et al. [1996b] and Lee et al. [1996]. Both approaches directly accelerate particles out of the pickup ion “thermal” pool. However, the MRI mechanism is found to produce high energies for pickup ions, and a very flat spectrum, and to have an injection efficiency which decreases with increasing particle mass. Unfortunately, present models of MRI acceleration are either purely analytic [Lee et al., 1996] or quasi-analytic [Zank et al., 1996b] and treat the pickup ions as test particles and use an analytic description for pickup ion orbits in a very idealized shock geometry. Zilbersher and Gedalin [1997] presented further analysis of the MRI mechanism together with some direct test particle tracing simulations. These simulations confirmed the predictions of the Zank et al. and Lee et al. theory besides exploring certain configurations that were not accessible analytically. While the issue of shock structure was addressed, this was primarily in the context of quasi-perpendicular shocks, and no extensive parameter study was presented. The purpose of this paper is therefore to investigate more completely the role that both shock structure and strong turbulence play on the MRI mechanism while remaining, for the present, within the limit of test particle pickup ions.

The heating and acceleration of ions are influenced by the character of the following processes: the source of pickup ions (PIs) in regions of mass loading and in the shock transition layer, i.e., the region between the upstream and downstream states (the foreshock, ramp, and overshoot), and the dynamics of the electron-proton subshock (i.e., whether the subshock is resistive or dispersive, whether it is subcritical or supercritical [Galeev et al., 1985], whether its structure is stationary or experiences cyclical reconstruction in time, or whether the subshock structure is modified by a whistler precursor [Galeev et al., 1991; Lipatov, 1994]). The heating and acceleration of ions may result from dissipation processes associated with high-frequency electrostatic and low-frequency electromagnetic instabilities at the shock current layer [see e.g., Winske, 1985]. Unfortunately, self-consistent simulations of quasi-perpendicular shocks [e.g., Leroy et al., 1982; Quest, 1985, 1986; Forslund et al., 1984; Tokar et al., 1986; Lembege and Dawson, 1989; Lipatov and Lobatchev, 1996], which may include PIs [Galeev et al., 1985; Lipatov and Syrovatskii, 1987; Omid and Winske, 1987; Liewer et al., 1993, 1995; Giacalone et al., 1994; Kucharek and Scholer, 1995], have

yet to demonstrate any significant acceleration of solar wind protons and PIs by MRI-like processes in the absence of either strong wave generation or externally imposed high levels of MHD turbulence. To understand the absence of accelerated PIs in the simulations, it is required that two issues be addressed. As noted above already, the first issue concerns the reasonableness of the quasi-analytic formulation of the PI reflection and subsequent acceleration process at idealized shocks. The second issue is whether the shock length scales in the simulations (and by implication the time and spatial scales) are sufficiently fine to address the acceleration of PIs at a shock by the MRI mechanism, which requires that the subshock be resolved on electron rather than ion inertial length scales. As we show, the possible lack of a strongly accelerated PI component in the various simulations may be due to an insufficiently strong electron-proton subshock, an insufficiently small subshock thickness, and time and space steps of integration which are too large. In Sections 3.1 and 3.2 we use a particle-mesh code to investigate in detail the dynamics of PIs in a structured shock front, as well as the effects of shock obliquity.

Yet another issue which needs to be considered more carefully than was done in the work of Zank et al. [1996b] and Lee et al. [1996] is the role of PI scattering and transport by low-frequency turbulence. Both theory and simulations show that the initial ring-beam distribution of PIs is unstable to the generation of Alfvén waves and magnetosonic modes [Wu and Davidson, 1972; Sagdeev et al., 1986; Wu et al., 1986; Winske and Gary, 1986; Winske et al., 1985; Galeev and Lipatov, 1984; Galeev et al., 1987]. These waves then scatter the PIs onto a bispherical shell in velocity space centered on $\pm V_A$ (the Alfvén speed) with radii u_{SW} (the local solar wind flow speed). As discussed by Zank et al. [1995, 1996b], it is the bispherical form of the PI distribution that makes MRI acceleration at interplanetary shocks and the heliospheric termination shock particularly attractive. Thus the MRI mechanism relies on the presence of low-frequency turbulence to scatter the initial PI ring-beam distribution onto a bispherical shell yet, at the same time, assumes that the scattering is not so strong as to disrupt the trapping of the PI between the particle Lorentz force and the shock electrostatic potential jump.

Besides influencing the efficacy of MRI acceleration, the presence of strong turbulence has implications for particle injection and the subsequent acceleration of low-energy PIs for Fermi acceleration at quasi-perpendicular shocks, as discussed by Giacalone et al. [1994]. These authors include ad hoc scattering perpendicular to the magnetic field, which allows PIs to diffuse across field lines. Giacalone et al. find that even at perpendicular shocks, PIs can be injected and accelerated to fairly high energies rather rapidly ($v/U_1 \approx 20$, where v denotes particle velocity and U_1 denotes the bulk flow speed) but that thermal solar wind ions cannot be injected and accelerated unless a very large (and most probably unrealistic) scattering level is assumed.

It is apparent therefore that PI scattering by low-frequency turbulence needs to be investigated carefully in the context of particle acceleration and injection by the MRI mechanism, and this is discussed in Section 3.3.

The remainder of the paper considers MRI acceleration at oblique shocks, the acceleration of pickup He^+ (Section 3.4), and the effect of shock ramp thickness on the maximum energy gain that can be expected for a particle (Section 3.5).

2. Formulation of the Problem and the Mathematical Model

The object of this paper is to study the energization of PIs at interplanetary shocks and the termination shock on the basis of a reduced (in spatial dimension) three-dimensional (3-D) particle-mesh (hybrid) code. Our goals are twofold: (1) The use of a particle-mesh code will allow us to study the dynamics of PIs in structured and turbulent shocks and thus to extend the previous analytic studies of *Zank et al.* [1996b] and *Lee et al.* [1996]. (2) The particle-mesh approach will also provide valuable insight into what kind of resolution and shock ramp thickness is needed to perform self-consistent simulations of the MRI acceleration of PIs. For this reason we study PI dynamics inside a shock transition layer with a fixed electromagnetic field profile. To simulate the acceleration of PIs inside a fixed shock transition layer, we use a 3-D hybrid code developed by *Lipatov* [1996]. This code is based on a particle-mesh method with an implicit calculation of the electric field, but in the present simulation, we do not update the electro-

magnetic field. The equation describing PI motion is integrated using a leapfrog scheme, and a 3-D linear weighting function is used to interpolate the grid values of the electromagnetic field at an ion location. Although in the present report we study only one-dimensional (1-D) and two-dimensional (2D) configurations, we use a 3-D hybrid code because this code is to be used in subsequent self-consistent simulations of the MRI acceleration problem. It should be mentioned here that 1- and 2-D simulations may give results which differ from those of a fully 3-D simulation [*Jokipii et al.*, 1993]. Some of the test particle simulations discussed here were repeated using 1- and 2-D versions of our hybrid code in order to effect a comparison with the quasi three-dimensional test particle simulations.

The basic idea of acceleration by the multiple reflection of PIs at the shock ramp is easily explained. On the PI shell distribution in the shock frame, a fraction of the PI population has so little kinetic energy that they can be reflected by the shock electrostatic potential jump inside the ramp, illustrated in Figure 1 [*Zank et al.*, 1996b]. This population of ions then drifts along the shock front surface, being multiply reflected at the shock ramp and trapped by the upstream particle Lorentz force and the electrostatic potential jump. The time spent upstream of the shock determines the maximum energy gain for a trapped PI, and this results from a balance between the particle Lorentz force and the gradient of the electrostatic potential.

In our simulation we use a 3-D computational box with the PI flow in the z direction. The unperturbed field is given at the left boundary, $z = 0$, and the incoming PI flow is generated by a given flux of a shell

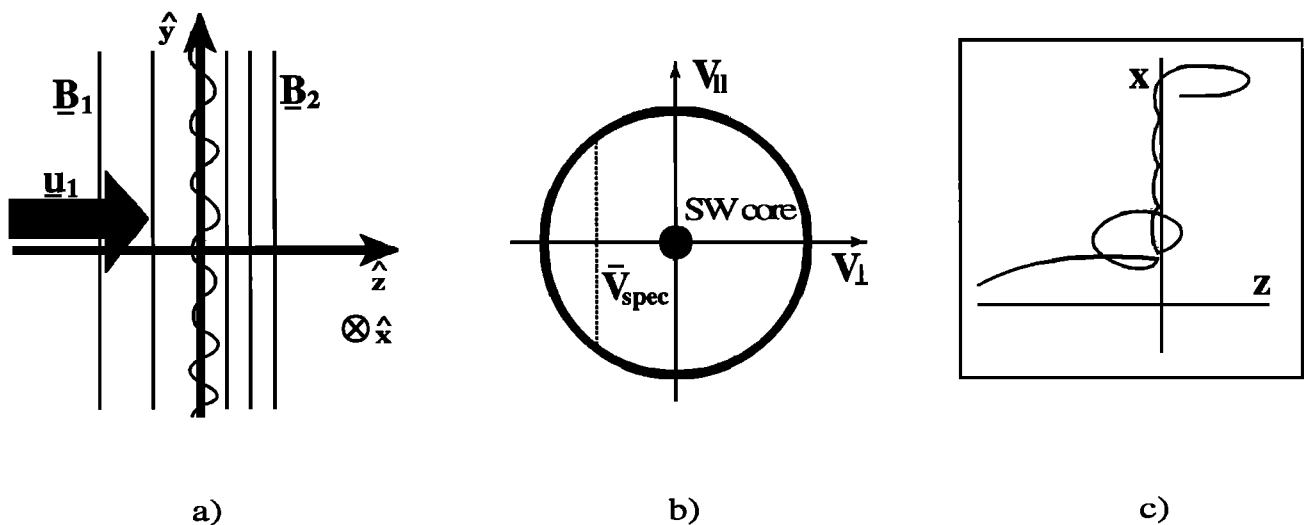


Figure 1. (a) Geometry of a quasi-perpendicular shock located at $z = 0$. The stream flow \underline{u} is parallel to the shock normal, the magnetic field \underline{B} lies along or oblique to \hat{y} , and the induced electric field is in the \hat{x} direction. The subscripts 1 and 2 denote upstream and downstream of the shock, respectively. (b) Schematic of the idealized shell distribution assumed for pickup ions (PIs) in the fluid frame. The cold solar wind (SW) core is represented by the heavy dot at the origin, and \bar{V}_{spec} corresponds to the normalized transformed specular reflection velocity below which PIs are reflected by the electrostatic shock potential barrier. (c) Example of integrated individual PI at a perpendicular shock located at $z = 0$ with an assumed step-like electrostatic cross-shock potential [*Zank et al.*, 1996b].

distribution of PIs. A free escape condition for PIs is set at the right boundary, $z = D_z$. At the other boundaries ($x = 0$, $x = D_x$, $y = 0$, and $y = D_y$), we use a cyclical condition for all parameters.

At the initial time the density profile of the PIs satisfies the Rankine-Hugoniot relation for a perpendicular shock,

$$\frac{n_{i2}}{n_{i1}} = \frac{|B_{\tau 2}|}{|B_{\tau 1}|} = \frac{U_{ni1}}{U_{ni2}} \equiv r \quad B_{n2} = B_{n1}, \quad (1)$$

the electric field satisfies the relation

$$E_{\tau 2} = E_{\tau 1} \quad E_{n2} - E_{n1} = -L_{\text{ramp}}^{-1} \Delta \phi_0, \quad (2)$$

and the value of the magnetic and the motional electric field at the left boundary is given by the parameters of the incoming flow

$$B = b_0 \quad E_{\text{mot}} = -\frac{U_{ni} \times b_0}{c} \quad (3)$$

where n_i denotes the PI number density, B and E denote the prescribed components of the magnetic and electric fields, U_{ni} is the component of the PI bulk velocity (equal to the bulk velocity of the thermal plasma), and r is the shock compression ratio. The subscripts n and τ denote components of the vector field which are perpendicular or tangential to the shock surface. The subscript 1 (2) denotes upstream (downstream) of the fixed shock. The initial PI distribution is a shell in velocity space, which we assume to have been thickened. The interior shell radius is taken to be $V_{\text{int}} \equiv v/U_{i1} = 1$, and that of the exterior shell is $V_{\text{ext}} = 1.2-1.5$, where v denotes particle velocity. This is not a very sensitive assumption. The thermal veloc-

ity of PIs (in the solar wind frame) is assumed to satisfy the adiabatic law initially, i.e.,

$$v_{th,2}/v_{th,1} = r^{(\gamma-1)/2}, \quad (4)$$

where γ is an effective adiabatic constant ($\gamma = 5/3$). In our simulation we use both the step-like (with a finite ramp thickness L_{ramp} , the dotted line in Figure 2) and the structured profiles illustrated in Figure 2 for the shock magnetic field and electrostatic potential. The ramp thickness, foot width, and the amplitude of both the electrostatic potential and ramp are prescribed parameters.

The jump in the electrostatic potential at the shock front may be estimated from the electron momentum equation. On defining $d\phi/dz = -E_z$, we obtain

$$e\Delta\phi_0 = \int_{z_1}^{z_2} \frac{eV_{iz}B_y}{c} d\xi + \int_{B_1}^{B_2} \frac{dB^2}{8\pi n} + \int_{p_{e1}}^{p_{e2}} \frac{dp_e}{n} \\ \equiv e(\Delta\phi_u + \Delta\phi_B + \Delta\phi_p), \quad (5)$$

where $\Delta\phi_u$, $\Delta\phi_B$, and $\Delta\phi_p$ possess different time-scales and spatial scales. However, in all our test particle simulations, the jump in electrostatic potential is chosen (for simplicity) by balancing the proton kinetic energy and the potential energy across the ramp of the shock, i.e.,

$$0.5 \frac{M_{PI} U_1^2}{2} = -e\Delta\phi_0, \quad (6)$$

where M_{PI} denotes PI mass, e denotes the electron charge and ϕ_0 denotes the electrostatic potential. Note that in all our simulations the motional electric field is taken to be a constant inside the computational box.

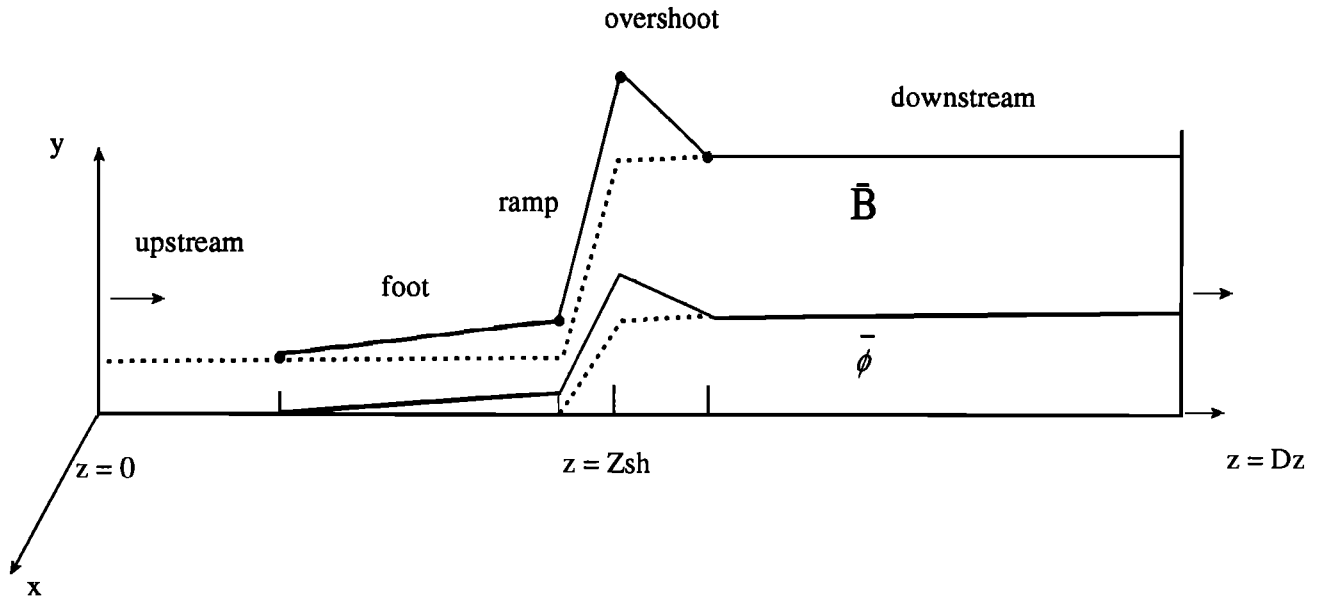


Figure 2. Geometry of the computational box. The incoming flux is at the left boundary $z = 0$. At the right boundary, $z = D_z$, PIs are allowed to escape freely. Typical profiles of the magnetic field and electrostatic potential are shown. The dotted line corresponds to the step-like profile with a ramp of finite thickness. The solid line corresponds to a structured shock profile.

We used a 1000- to 4000-node (in the case of H^+) and a 16000-node (in the case of He^+) grid in the z direction, a 3- to 15-node grid in the x direction, a 3-node grid in the y direction, and $N_p = (3 - 12) \times 10^5$ macro-Pis. The size of the computational box is $D_z = 5r_{ci}$, $D_x = (0.3 - 1.5)r_{ci}$, $D_y = 0.3r_{ci}$, where r_{ci} is the PI cyclotron radius, $T_{ci} = 2\pi/\Omega_i$, and Ω_i the PI gyrofrequency. The space and time steps used in the simulations are $\Delta z = (0.00125 - 0.005)r_{ci}$ and $\Delta t = 2.5 \times (10^{-4} - 10^{-5})T_{ci}$, and the minimum ramp thickness is $L_{ramp} = 0.01r_{ci}$. Such small spatial scales and timescales were chosen to resolve the ramp on an electron inertial length scale and to provide an accurate calculation of PI trajectories as they are transmitted across the ramp. As was discussed by Zank *et al.* [1996b] and Lee *et al.* [1996], assumptions about L_{ramp} are critical to the mechanism of MRI acceleration. However, our current (not very good) understanding of the microstructure of quasi-perpendicular shocks (derived from ISEE measurements of the Earth's bow shock and hybrid simulations) is that the shock consists of a very narrow ramp whose thickness scales with the electron inertial length c/ω_{pe} [Kennel *et al.*, 1985] together with a foot and overshoot whose length scales are determined by ion kinetic effects (see Goodrich [1985] for a review). Since the ramp is dominated by resistive or electron inertial effects, it possesses the steepest gradients and is the relevant scale for L_{ramp} . Further support for this assumption comes from the observational estimates of shock ramp widths presented by Scudder *et al.* [1986] and Balikhin *et al.* [1995]. Both sets of authors find that the ramp width is much less than the ion inertial length. Numerical simulations of high Mach number perpendicular shocks by Tokar *et al.* [1986] find that the ramp width can become as small as an electron gyroradius. Finally, Newbury and Russell [1994] observed a highly quasi-perpendicular ($\theta \approx 85^\circ$) supercritical shock with a ramp width of $\sim 2c/\omega_{pe}$. These results suggest that the assumption of a ramp width which scales with the electron inertial length might be reasonable.

3. Results of the Simulation

The calculations were made with the following plasma parameters, which are expected of the solar wind in the transition layer of the termination shock: $M_A = 5$, $\beta_p = \beta_e = 0.1$, and $r = 4$, where M_A is the Alfvén Mach Number, $\beta_{p(e)}$ denotes the solar wind proton (electron) plasma beta, and r is the jump in the magnetic field at the quasi-perpendicular shock front. In the test particle simulations it is important to use the jump of the magnetic field at the overshoot, which is higher than the Rankine-Hugoniot value. For simplicity we use the same value of r ($r = 4$) in all our simulations. As discussed by Zank *et al.* [1996b], the shock compression ratio is not an important parameter in the MRI acceleration mechanism.

3.1. The θ_{bn} Dependence of the Energy Spectrum of Accelerated H^+ Ions

Here we consider only the step-like profile illustrated in Figure 2 and vary the obliquity of the shock since

PI trajectories depend sensitively on the angle between the magnetic field and a shock front normal θ_{bn} . For $\theta_{bn} = 90^\circ$ the distribution function of PIs at different locations relative to the shock ramp is plotted in Figure 3. Figure 3a shows the projected PI distribution in the plane $(v_{\perp 1}, v_{\perp 2})$ at various distances from the shock ramp, where $v_{\perp 1}$ and $v_{\perp 2}$ are the velocity components, which are perpendicular to the magnetic field. The distributions in Figure 3 are arranged in ascending order from the bottom according to position as follows: upstream foot (bottom distribution), on the shock front, just downstream of the shock, and, the top distribution, far downstream. The bottom distribution illustrates a very typical distribution, which results from ion reflection at a perpendicular shock. Such distributions are seen at virtually all quasi-perpendicular shocks, both observationally [e.g., Schopke, 1995] and in simulations [e.g., Leroy *et al.*, 1982], and they contribute essentially to the formation of the ion shock foot. If the number and energy density of the reflected PIs were sufficiently high at the termination shock, the foot structure and length scales would be determined primarily by reflected PIs rather than by the colder more numerous solar wind protons [Liewer *et al.*, 1993; Zank *et al.*, 1996b]. The second distribution from the bottom shows the PI distribution at the shock ramp, and a strong transverse acceleration of PIs along the shock front is evident with the formation of an extended "tongue" along $v_{\perp 2}$. Finally, phase mixing occurs far downstream. Figure 3b shows the projection of the PI distribution onto the $(v_{\perp}, v_{\parallel})$ plane, where v_{\parallel} is the velocity component, which is parallel to the magnetic field.

The PI energy spectrum has two parts, as discussed by Zank *et al.* [1996b]: a shell-like distribution with an energy cut-off at about $E_0 = mU_1^2/2$ in the solar wind frame and an accelerated PI component which emerges from the shell distribution as a hard, flat power law spectrum. The accelerated PI energy spectrum may be approximated by the power law $F_i \propto dN/N \approx (E/E_0)^{-k}$, where the energy E is calculated in the solar wind frame and N denotes the PI number density. The top spectra in Figures 4a and 4b show the PI energy spectrum for $\theta_{bn} = 90^\circ$. In this case, the index k is ~ 1.2 . The similarity between the spectra produced by the particle-mesh simulation here and those obtained from the quasi-analytical approach of Zank *et al.* [1996b] is close. The spectrum produced by the MRI mechanism is much harder than that expected of diffusive shock acceleration, which would produce an E^{-2} spectrum for the shock compression ratio used in our simulations. Also, as discussed in Section 2 of Zank *et al.* [1996b], diffusive shock acceleration at a perpendicular shock imposes severe energy constraints on the particles to be accelerated, constraints which are absent for MRI acceleration.

The remaining spectra in Figures 4a and 4b illustrate the evolution of the PI energy spectrum as θ_{bn} is decreased from 90° . Initially, as θ_{bn} changes, the accelerated PI power law spectrum becomes considerably harder ($k = 0.92$ when $\theta_{bn} = 87.5^\circ$ (not plotted) to

$$\theta_{bn} = 90^\circ$$

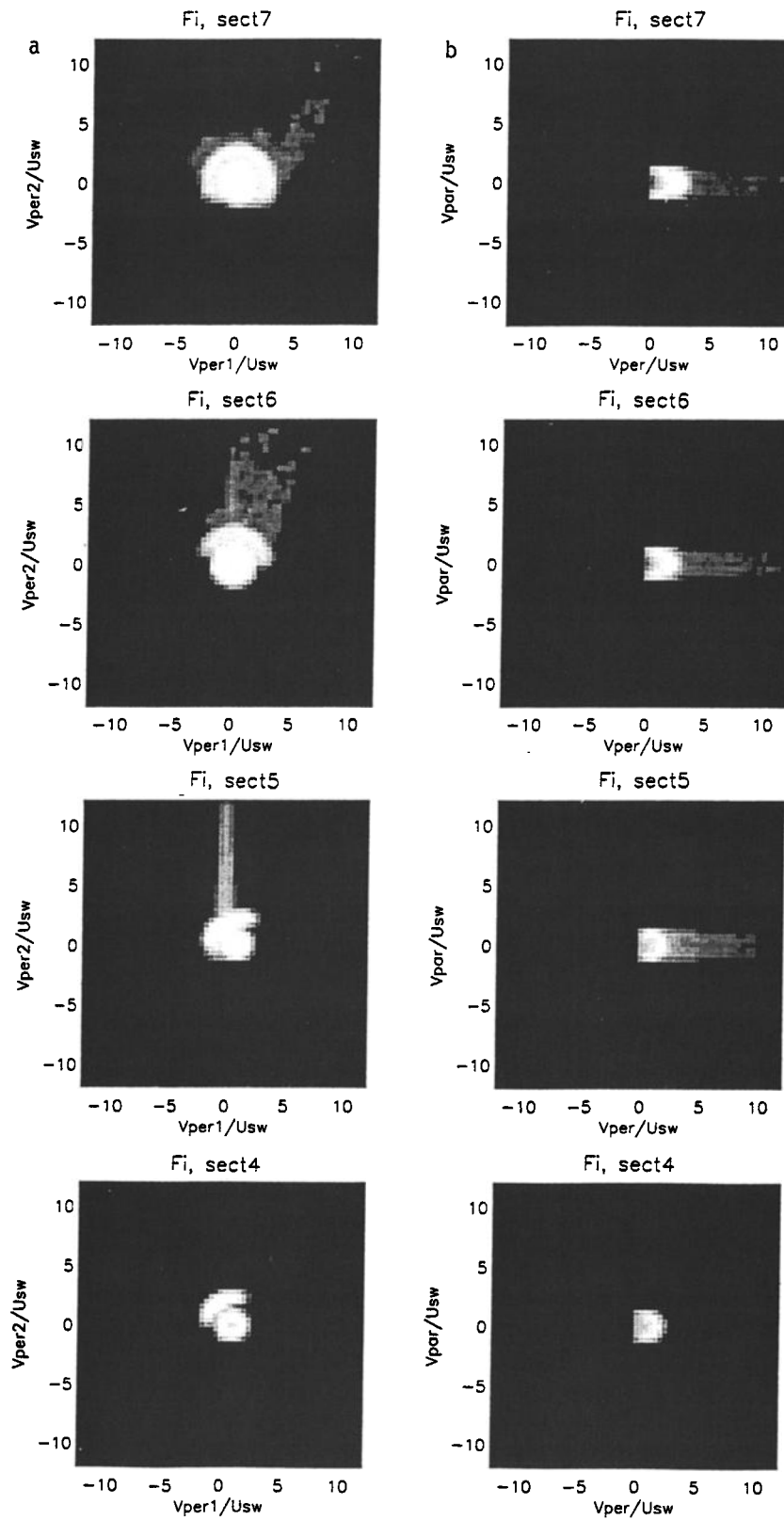


Figure 3. The projection of the PI distribution onto the velocity plane for spatial sections ranging from downstream to upstream in the case of a step-like transition layer ($\theta_{bn} = 90^\circ$). Here v_\perp and v_\parallel are the velocity components perpendicular to and parallel to the magnetic field, respectively. F_i denotes the PI velocity distribution.

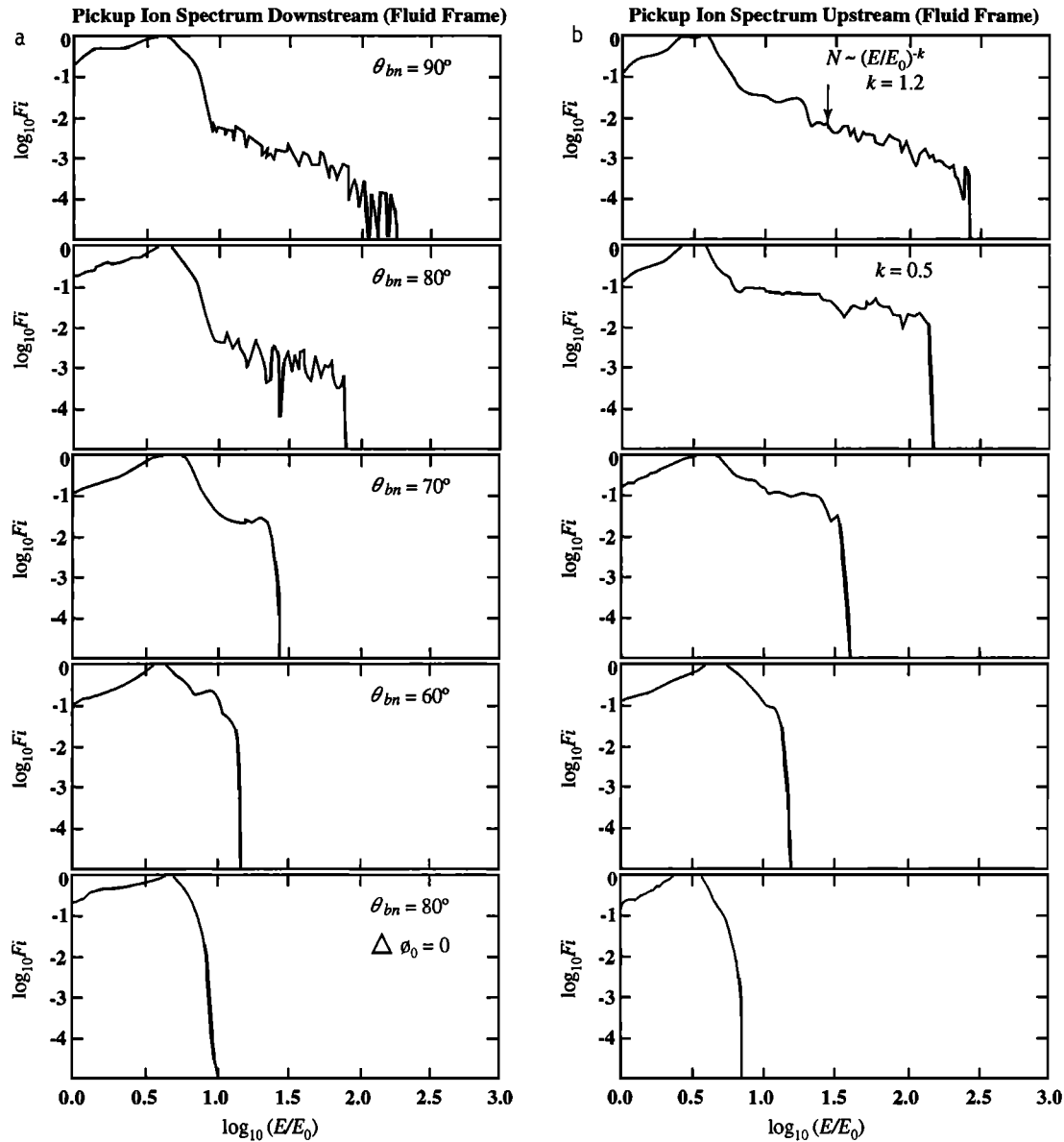


Figure 4. The θ_{bn} dependence of the energy spectrum of accelerated PIs in the fluid frame for (a) particles downstream of the shock and (b) upstream particles.

$k = 0.5$ when $\theta_{bn} = 80^\circ$). The hardening of the energy spectrum is due to the motion of PIs along the magnetic field. As the shock obliquity increases, a reflected PI will spend a proportionally greater time in the motional electric field than would the same reflected PI in a purely perpendicular shock. Thus the PI reflected by the oblique shock will acquire a little more energy than its counterpart at the perpendicular shock. Since most reflected PIs experience the initial reflection only, gaining sufficient energy in the single encounter to overcome the shock electrostatic potential on the subsequent meeting, more PIs reflected at a slightly oblique shock gain greater energy than they otherwise would at a perpendicular shock. Conversely, fewer multiple reflections can now occur, but the multiply reflected PIs will similarly gain comparatively more energy than their per-

pendicular shock counterparts. Overall, the effect of increasing the shock obliquity is twofold: it must lead to a flattening of the accelerated ion spectrum, but it also reduces the ability of PIs to reflect multiple times. The distribution function of PIs just before and behind (Figure 5) the ramp shows the dynamics of PIs for the case $\theta_{bn} = 80^\circ$.

As the reflected PIs become increasingly energetic at an oblique shock, the possibility of their escaping upstream becomes greater. This factor will affect the maximum energies that can be gained by reflected PIs. Of course, increasing θ_{bn} beyond some critical obliquity results in the escape of all reflected PIs upstream along the magnetic field. As shown in the $\theta_{bn} = 60^\circ$ and $\theta_{bn} = 70^\circ$ examples of Figure 4 and also in Figure 6, a strong beam of reflected ions in the upstream direction

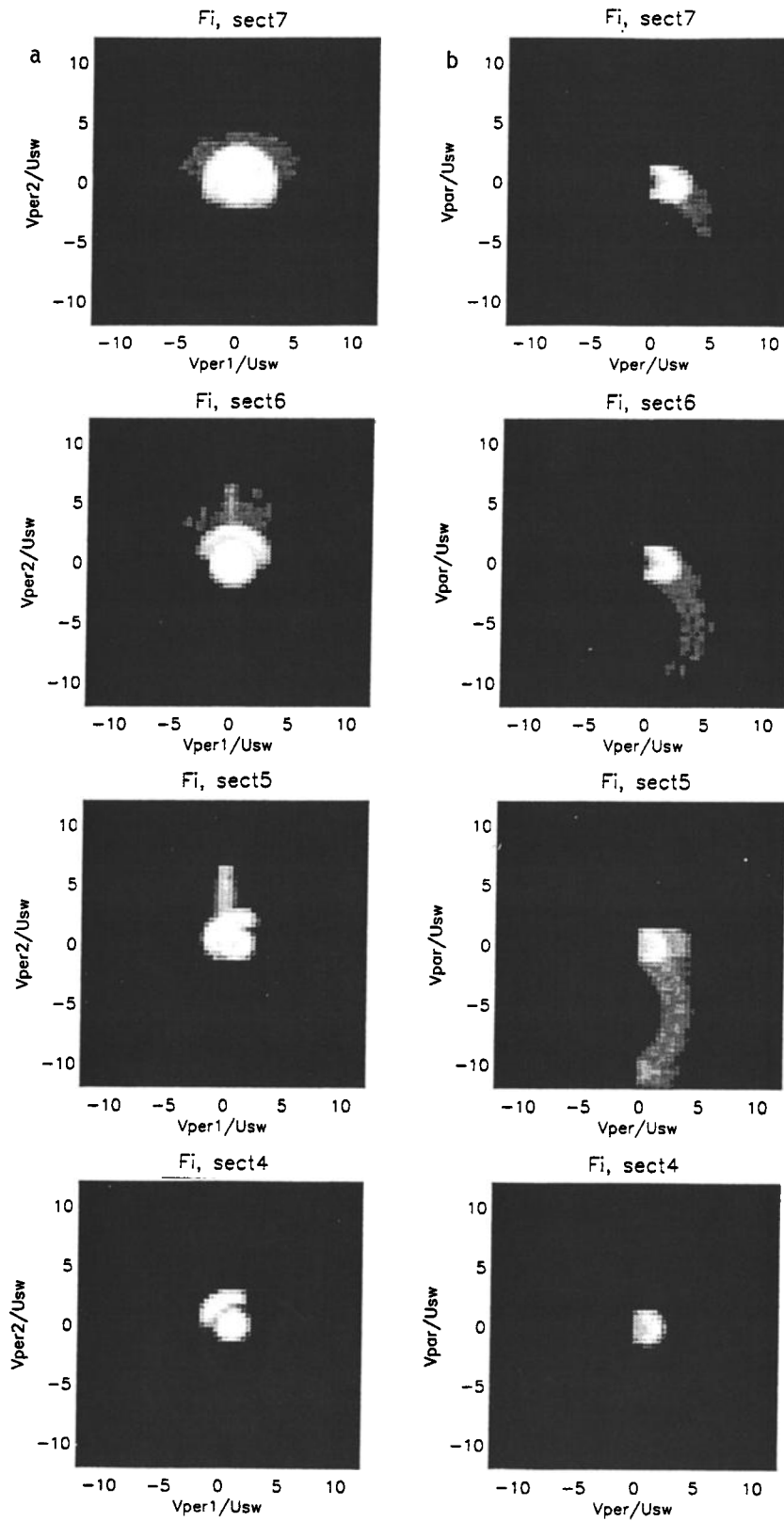


Figure 5. The projection of the PI distribution onto the velocity plane for spatial sections behind and before the ramp when $\theta_{bn} = 80^\circ$. Here v_\perp and v_\parallel are the velocity components perpendicular to and parallel to the axis y , respectively.

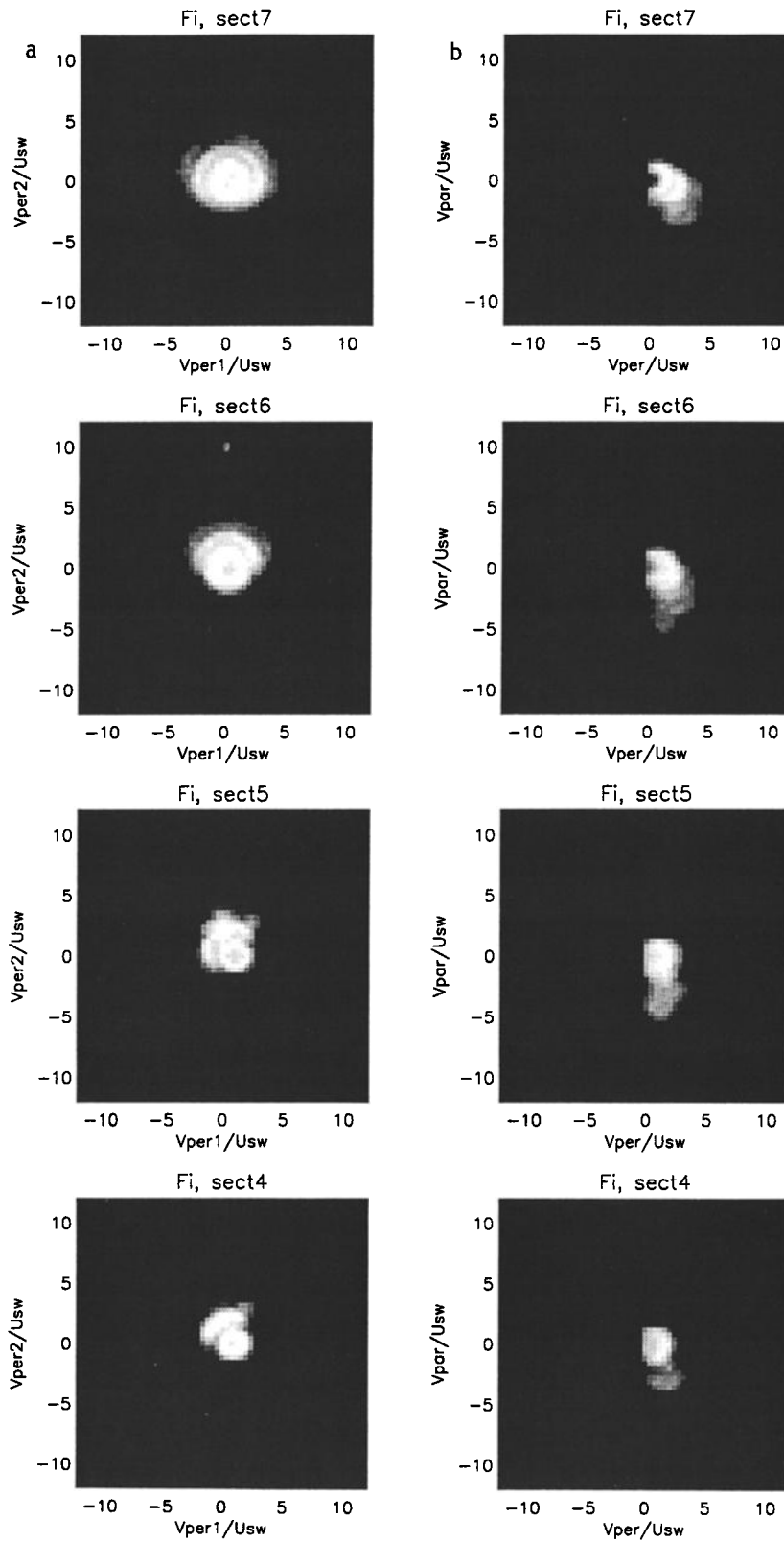


Figure 6. The projection of the PI distribution onto the velocity plane for spatial sections behind and before the ramp when $\theta_{bn} = 70^\circ$. Here v_\perp and v_\parallel are the velocity components perpendicular to and parallel to the axis y , respectively.

is formed, and the maximum energy of the accelerated PIs is much lower than that seen in the $\theta = 90^\circ$ simulation.

Finally, the bottom spectra in Figures 4a and 4b illustrate a simulation with $\theta_{bn} = 80^\circ$ but now without an electrostatic potential jump. This example demonstrates the presence of PIs leaking upstream from downstream, and it shows too that without the electrostatic potential jump, no acceleration of the incoming ions at the shock ramp occurs.

3.2. Pickup Ion Acceleration at Structured Perpendicular Shocks

To study the effect of a complex structured shock transition layer on the acceleration of PIs, we took into account the results of hybrid [Quest, 1986] and full particle [Lipatov and Lobachev, 1996] simulations of collisionless shocks in a plasma possessing a small proton plasma beta, $\beta_p = 0.1$. This plasma beta parameter, the ratio of thermal pressure to magnetic pressure, is computed using the cold solar wind protons and electrons only; the inclusion of the hot (~ 1 keV) PI component would increase the total plasma beta to ~ 3 [Zank et al., 1995]. The magnetic field profile is approximated by the solid labeled piecewise linear function il-

lustrated in Figure 2, and our parameters are chosen to be $b_{up} = b_0$, $b_{foot} = (1.25 \div 1.5)b_0$, $b_{over} = 5b_0$, and $b_{down} = 4b_0$, where b_0 is the value of the magnetic field in the solar wind. The subscripts up, foot, over, and down correspond to the maximum values of the magnetic field in upstream, foot, overshoot, and downstream, respectively. The electrostatic potential is approximated by a similar piecewise linear function, also illustrated in Figure 2 as a solid labeled line, with the parameterization $\phi_{up} = 0$, $\phi_{foot} = (0.05 \div 0.1)\Delta\phi_0$, $\phi_{ramp} = \Delta\phi_0$, and $\phi_{down} = 0.66\Delta\phi_0$, where ϕ_0 is a jump of the electrostatic potential inside the ramp (see section 2). The sizes of the shock foot, ramp, and overshoot were chosen to be $L_{foot} = 0.5r_{ci}$, $L_{ramp} = 0.01r_{ci}$, and $L_{over} = 0.25r_{ci}$. The motional electric field was chosen as a constant inside the computational box. Results from three simulations are illustrated in Figure 7. Figure 7a, included for reference, shows the PI accelerated spectrum at a step-like transition layer. Figure 7c is distinguished by the assumed strength of the magnetic field and electrostatic potential in the shock foot.

For the weak shock foot, i.e., that with the smaller electrostatic potential, we obtain approximately the same accelerated PI energy spectrum downstream of

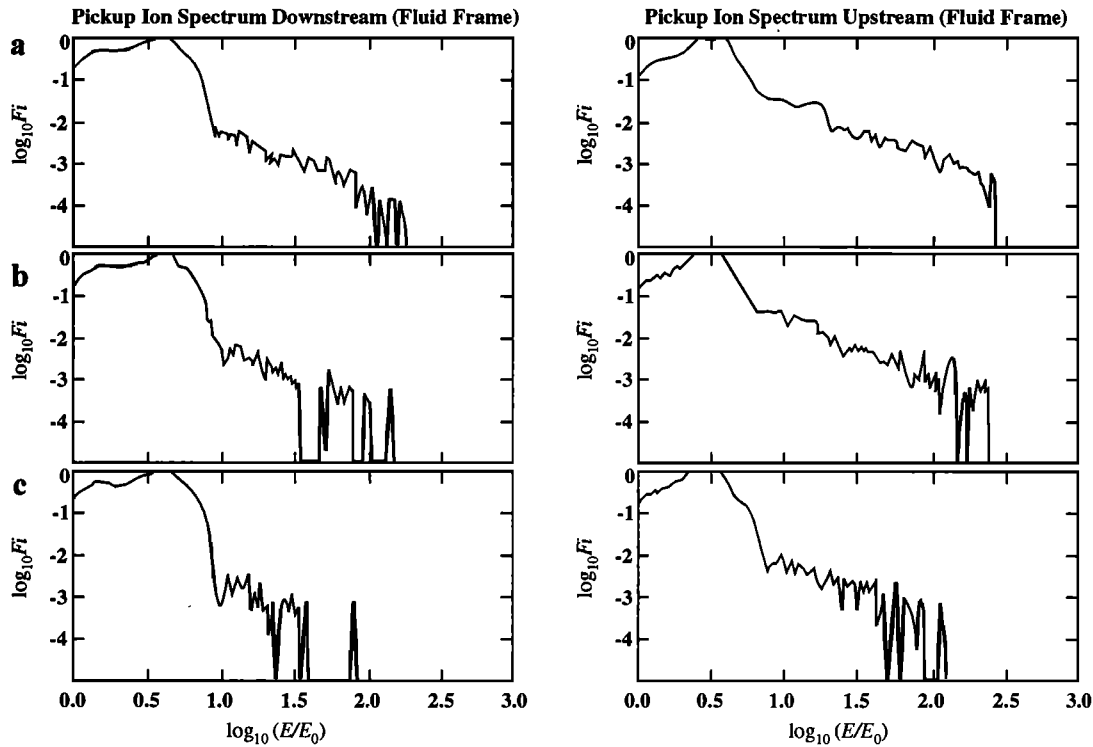


Figure 7. The PI energy spectrum at a structured perpendicular shock for (a) a step-like shock transition layer, (b) a weakly structured shock transition layer, and (c) a strongly structured shock transition layer. Figure 7b used the following parameters; for the magnetic field profile $b_{up} = b_0$, $b_{foot} = 1.25b_0$, $b_{over} = 5b_0$, and $b_{down} = 4b_0$, and for the electrostatic potential profile $\phi_{up} = 0$, $\phi_{foot} = 0.05\Delta\phi_0$, $\phi_{ramp} = \Delta\phi_0$, and $\phi_{down} = 0.66\Delta\phi_0$. The sizes of the shock foot, ramp and overshoot were chosen to be $L_{foot} = 0.5r_{ci}$, $L_{ramp} = 0.01r_{ci}$, and $L_{over} = 0.25r_{ci}$. The subscripts up, foot, over, and down correspond to upstream, foot, overshoot and downstream respectively. For Figure 7c parameters of the magnetic field profile are $b_{up} = b_0$, $b_{foot} = 1.5b_0$, $b_{over} = 5b_0$, and $b_{down} = 4b_0$, and for the electrostatic potential $\phi_{up} = 0$, $\phi_{foot} = 0.1\Delta\phi_0$, $\phi_{ramp} = \Delta\phi_0$, and $\phi_{down} = 0.66\Delta\phi_0$.

the shock front (Figure 7b) as that obtained in the case of the step-like transition layer. However, increasing the electrostatic potential in the foot leads to a reduction in the maximum energy of accelerated PIs (Figure 7c) compared to that found in Figures 7a and 7b. The difference between the weak and strong shock foot cases is a consequence of the incident PIs experiencing some magnetic deceleration in the shock foot, which implies that ion reflection is no longer specular. Although the reflected ions may regain some energy in the foot, it is insufficient to render the process specular, and some intrinsic modification to the PI dynamics can therefore be expected when the shock foot is strong. Figure 8 shows the projected PI distribution onto the velocity plane. It is clear that the acceleration of PIs in a structured shock is somewhat weaker than that at a step-like transition layer. In the presence of a strong foot the spatial variation of the electrostatic potential may be comparable to that of the jump at the ramp, and hence we cannot expect a strong MRI acceleration under these circumstances.

3.3. Turbulence in the Shock Transition Layer of Perpendicular Shocks

To investigate the effect of electromagnetic waves and turbulence on the MRI acceleration of PIs, we conducted the following simulations using perpendicular shocks without structure. In the first series of simulations, we considered one-dimensional, external, stationary perturbations of the magnetic field throughout the shock layer (i.e., upstream, transition layer, and downstream). The fluctuations in the magnetic field and the electrostatic potential were chosen to vary as

$$b_x(z) = 0.2b_0 e^{imK_0 z} \quad b_y(z) = \bar{B}_y + 0.2b_0 e^{imK_0 z}$$

$$b_z(z) = 0.2b_0 e^{imK_0 z}, \quad \text{and} \quad \phi(z) = \bar{\phi} + 0.2\Delta\phi_0 e^{imK_0 z}.$$

The motional electric field was chosen as a constant $\mathbf{E}_{\text{mot}}(z) = (E_x, 0, 0) = \text{const}$, and the magnetic field satisfies the divergence condition $\nabla \cdot \mathbf{B} = 0$. The typical value of m ranges from $m = 5$ to $m = 50$ (in units of $K_0 = 2\pi/5r_{ci} = 2\pi\omega_{pi}/25c$), and \bar{B} and $\bar{\phi}$ are a step-like profile with a ramp of finite thickness, $L_{\text{ramp}} = 0.01r_{ci}$. The amplitude of the perturbations is 0.2 in accordance with an estimate of the level of background turbulence at the termination shock [Zank *et al.*, 1996a]. In this simulation we use a computational box with three grid points in the x and y directions. The results of the simulation are illustrated in Figure 9. Figure 9a is a reference spectrum corresponding to a simulation without any perturbations in \mathbf{b} or ϕ . Figure 9b shows the accelerated PI energy spectrum for the case of $m = 50$. The maximum energy gain downstream of the shock, although larger than that of the reference simulation, is a little less than that found from a simulation using $m = 5$. However, essentially the same power law index is recovered.

In the second series of simulations we used a one-dimensional random generator and a two-dimensional random generator to provide the random distribution

of perturbations for the magnetic field and the electrostatic potential. These profiles are chosen as (1)

$$b_x(z_i) = 0.4b_0\left(\frac{1}{2} - \xi_i\right) \quad b_y(z_i) = \bar{B} + 0.4b_0\left(\frac{1}{2} - \xi_i\right)$$

$$b_z(z_i) = 0, \quad \text{and} \quad \phi(z_i) = \bar{\phi} + 0.4\Delta\phi_0\left(\frac{1}{2} - \xi_i\right),$$

and (2)

$$\tilde{b}_x(x_i, z_i) = 0.4b_0\left(\frac{1}{2} - \xi_i\right) \quad \tilde{b}_y(x_i, z_i) = \bar{B} + 0.4b_0\left(\frac{1}{2} - \xi_i\right)$$

$$\tilde{b}_z(x_i, z_i) = 0.4b_0\left(\frac{1}{2} - \xi_i\right),$$

and

$$\phi(x_i, z_i) = \bar{\phi} + 0.4\Delta\phi_0\left(\frac{1}{2} - \xi_i\right),$$

where ξ_i are random numbers from the interval $[0, 1]$. To calculate the value of b and ϕ , we use the same generator of pseudorandom numbers for a set of grid points $\{z_i\}$ or $\{x_i, z_i\}$. Since the components of the magnetic field (\tilde{b}_x and \tilde{b}_z) do not satisfy the divergence condition, we made the following correction. Suppose that the magnetic field may be split into two parts, $\tilde{\mathbf{b}} = \nabla \times \mathbf{A} + \nabla G$. Then we can find G from the next equation,

$$\Delta G = \nabla_{x,z} \cdot \mathbf{b}_{x,z},$$

with a periodic boundary condition at $z = 0$ and $z = D_z$. At the boundaries $x = 0$ and $x = D_x$, we have periodic boundary conditions in all the simulations presented in this paper. The final divergence-free magnetic field is then calculated from the equations

$$b_x = \tilde{b}_x - \nabla_x G \quad b_y = \tilde{b}_y \quad b_z = \tilde{b}_z - \nabla_z G.$$

The motional electric field was chosen as a constant $\mathbf{E}_{\text{mot}}(x, z) = (E_x, 0, 0) = \text{const}$. Such a spectrum contains a wide range of wave vectors K , ranging from $K_{\text{min}} = 2\pi/5r_{ci} = 2\pi\omega_{pi}/25c$ to $K_{\text{max}} = 800\pi/r_{ci} = 160\pi\omega_{pi}/c$. This type of spectrum allows us to study the influence of turbulence on the PI dynamics and reflection in the vicinity of the small-scale shock ramp. In these simulations we use a computational box with 15 grid points and 3 grid points in the x and y directions, respectively.

Figures 9c and 9d show that in the presence of turbulence the power index k of the energy spectrum decreases upstream, but the maximum energy of the accelerated ions is slightly higher in the downstream region compared to that of the stationary reference simulation. Figure 10 shows the spatial profiles of the magnetic field component B_y , the electric field component E_x and the PI density n_i for a simulation using strong two-dimensional turbulence. It is clearly seen that the peak in PI density corresponds to accelerated PIs and that the peak is located inside the shock ramp. The formation of the peak in PI density inside the shock ramp was observed in all the simulations considered in this paper.

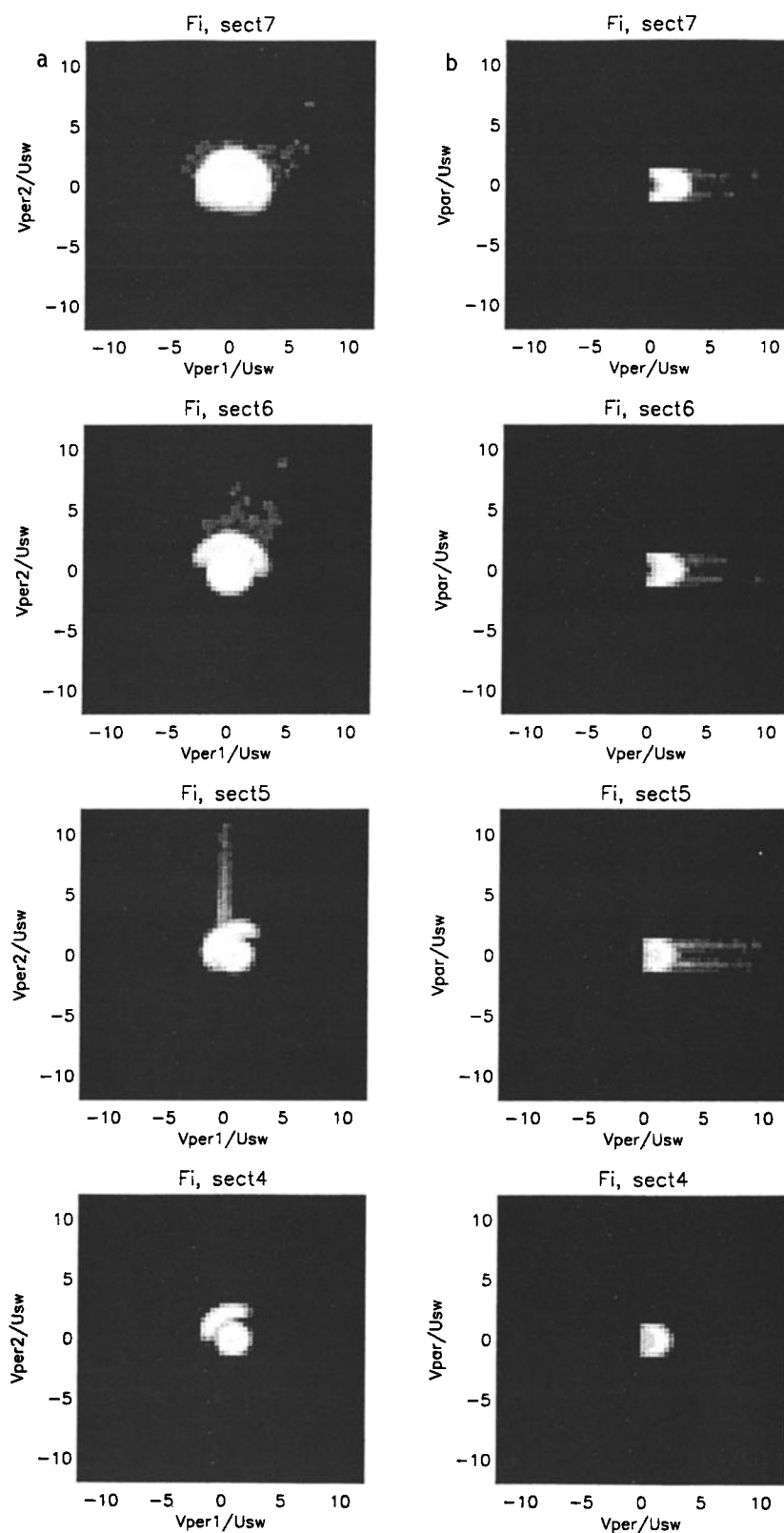


Figure 8. The projection of the PI distribution onto the velocity plane for regions behind and before the ramp in the case of a strongly structured shock and $\theta_{bn} = 90^\circ$. Here v_\perp and v_\parallel are the velocity components perpendicular to and parallel to the magnetic field, respectively.

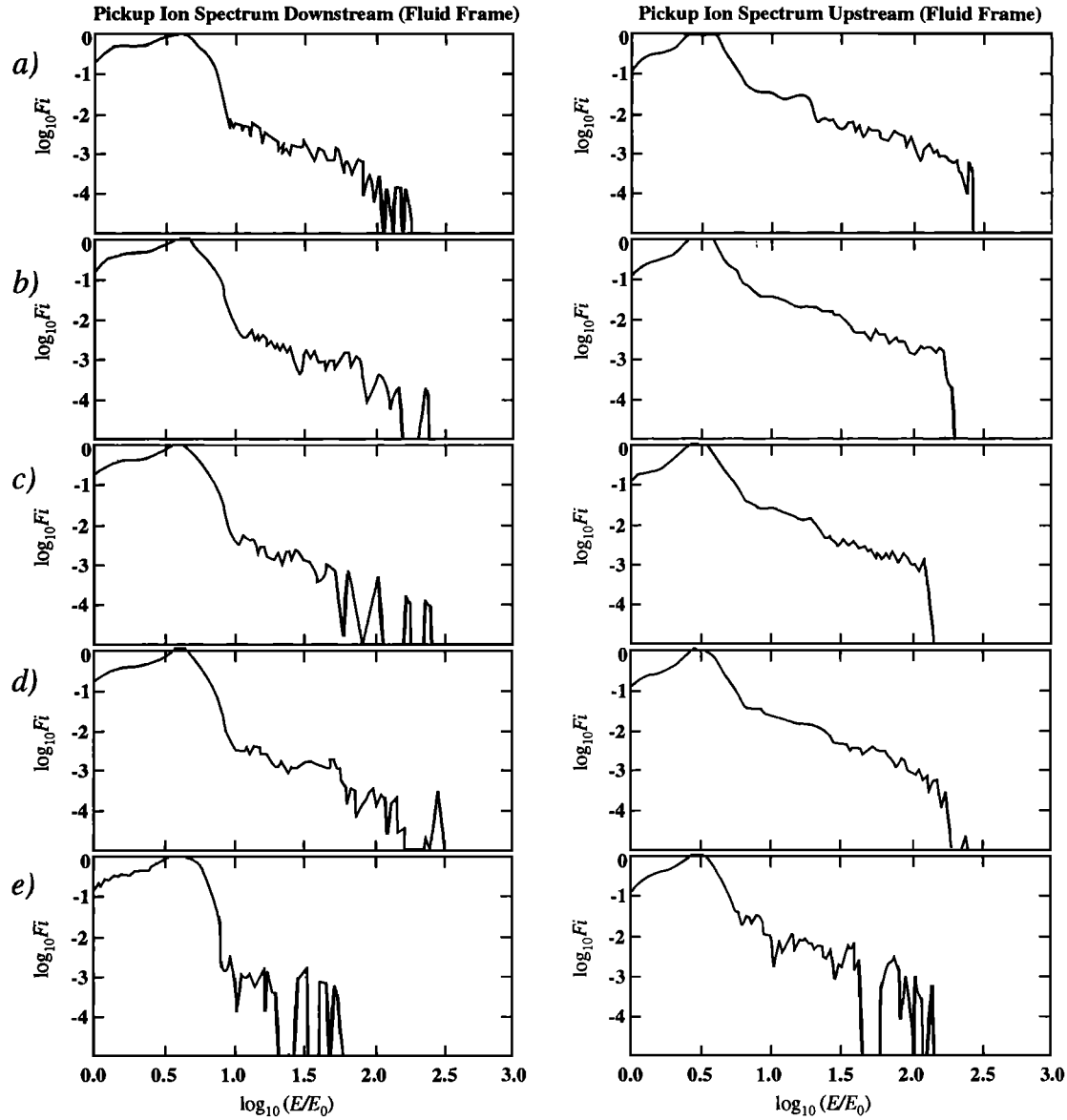


Figure 9. The effect of turbulence on the accelerated PI energy spectrum for (a) a step-like transition layer without external perturbations, (b) a steady state harmonic perturbation, (c) a one-dimensional (1-D) random perturbation of the electromagnetic field, (d) a two-dimensional (2-D) random perturbation of the electromagnetic field, and (e) a power law turbulent spectrum $P(K) \propto K^\alpha$.

In the third series of simulations we used a one-dimensional power spectrum for magnetosonic turbulence ($\mathbf{b} \parallel \mathbf{B}$, where $\mathbf{B} = (0, B_y, 0)$ is a step-like profile with a ramp of finite thickness, $L_{\text{ramp}} = 0.01r_{ci}$): $P(K) \propto K^{-1}$ for the wavelengths $K < K^*$ and $P(K) \propto K^{-5/3}$ for the wavelengths $K \geq K^*$ (where $K^* = \Omega_i/V_A = \omega_{pi}/c$, $\lambda^* = 2\pi c/\omega_{pi} = 2\pi r_{ci}/M_A$ and V_A is the Alfvén speed). These perturbations of the magnetic field were considered as a stationary wave packet propagating with the Alfvén speed in forward and opposite directions in the fluid frame. The turbulence level was chosen to have a value of $\epsilon = 0.2$, where $\epsilon b_0^2/2 = \sum_K b_K^2 b_0^2/2$ and b_0 is the value of the magnetic field in the solar wind. The motional electric

field was $\mathbf{E}_{\text{mot}}(z) = (E_x, 0, 0) = -\mathbf{U}_{n1} \times \mathbf{b}_0/c + \delta\mathbf{E}$, where the perturbation of the electric field $\delta\mathbf{E}$ was found from Faraday's law. The electrostatic potential was chosen as a step-like profile with a ramp thickness $L_{\text{ramp}} = 0.01r_{ci}$ (Figure 1b, dotted line). In these simulations we use a computational box with three grid points in the x and y directions. Figure 9e shows that the presence of power law turbulence reduces the maximum possible PI energy when compared to that of the unperturbed unstructured ramp example. However, a substantial energy gain is still possible, and a very hard power law spectrum occurs. Figure 11 shows the projection of the PI distribution onto the velocity plane in downstream and upstream regions. Here we see that the

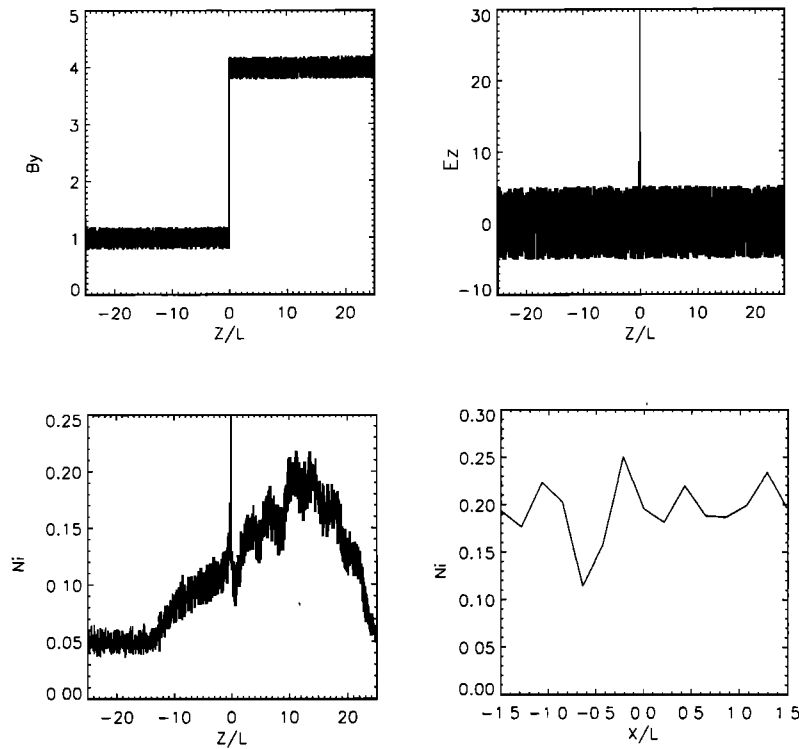


Figure 10. Typical profiles of the magnetic field component B_y , electric field component E_z and the pickup ion density n_i , in the presence of strong turbulence.

turbulence can produce some disruption of the tongue of accelerated PIs, and in particular, the intensity of the accelerated PIs is somewhat less than that of the nonturbulent mediated shock. It is important to recognize that our simulations address the influence of weak turbulence on the MRI acceleration mechanism on very short characteristic timescales only ($t_{\text{accel}} \approx T_{ci}$). This is because MRI acceleration is inherently a very rapid process; that is, the PI experiences energization over only several multiples of part of an ion gyroradius before it escapes the potential trap and is transmitted downstream. The long time simulation of PI acceleration ($t_{\text{accel}} \approx 100T_{ci}$) by strong electromagnetic fluctuations at quasi-perpendicular and oblique shocks [see, e.g., Giacalone *et al.*, 1994; Liewer *et al.*, 1993, 1995; Kucharek and Scholer, 1995] results in the Fermi acceleration of PIs and a quite different spectrum. It should be mentioned here that the use of a small number of grid points in the direction perpendicular to the magnetic field may suppress some effects, such as cross-field scattering of pickup ions, for example [Jokipii *et al.*, 1993].

3.4. MRI Acceleration of Pickup He^+

For these simulations a step-like profile of the perpendicular shock transition layer, equivalent to that of the H^+ case, was used. The size of the computational box is now taken to be $D_z = 5r_{ci, \text{He}^+}$, and the jump in electrostatic potential and ramp thickness is as before (i.e., as used for the acceleration of H^+). Since He^+ is heavier than H^+ , a smaller fraction of the incident

PI shell distribution is capable of experiencing multiple reflection at the shock electrostatic potential [Zank *et al.*, 1996b]. The injection efficiency of pickup He^+ is accordingly much less than that of pickup H^+ . However, the energy spectrum of accelerated He^+ PIs at the shock front in the fluid frame is described by the same power law, $F_i \approx (E/E_0)^{-k}$, with $k = 1.2 - 1.3$, and it is illustrated in Figure 12.

3.5. Shock Ramp Thickness and the Maximum Energy of Accelerated Pickup Ions at Perpendicular Shocks

The ramp thickness of collisionless shocks is a very important parameter since it effectively controls the process of MRI acceleration. In our simple model the normal component of the electric field is determined by the electrostatic potential. The particle Lorentz force $e\mathbf{v}_x \mathbf{B}$ may eventually exceed the force exerted by the electrostatic potential $-e\nabla\phi$, thus allowing the reflected ion to escape downstream. The maximum transverse velocity of accelerated ions may therefore be estimated by balancing the Lorentz force and the force exerted by the electrostatic potential [Zank *et al.*, 1996b], so that $\log_{10}(E_{\text{max}}/E_0) = 2\log_{10}[\eta(r-1)/M_A^2] - 2\log_{10}(L_{\text{ramp}}/r_{ci})$. The parameter η has been introduced to approximate the contribution to ϕ of the deflected bulk velocity u_n , which results from ion reflection at the shock ramp [Leroy, 1983]. Empirically, η is found to be ~ 2 or greater. Here we take $\eta = 2$. Figure 13 shows the dependence of the maximum energy

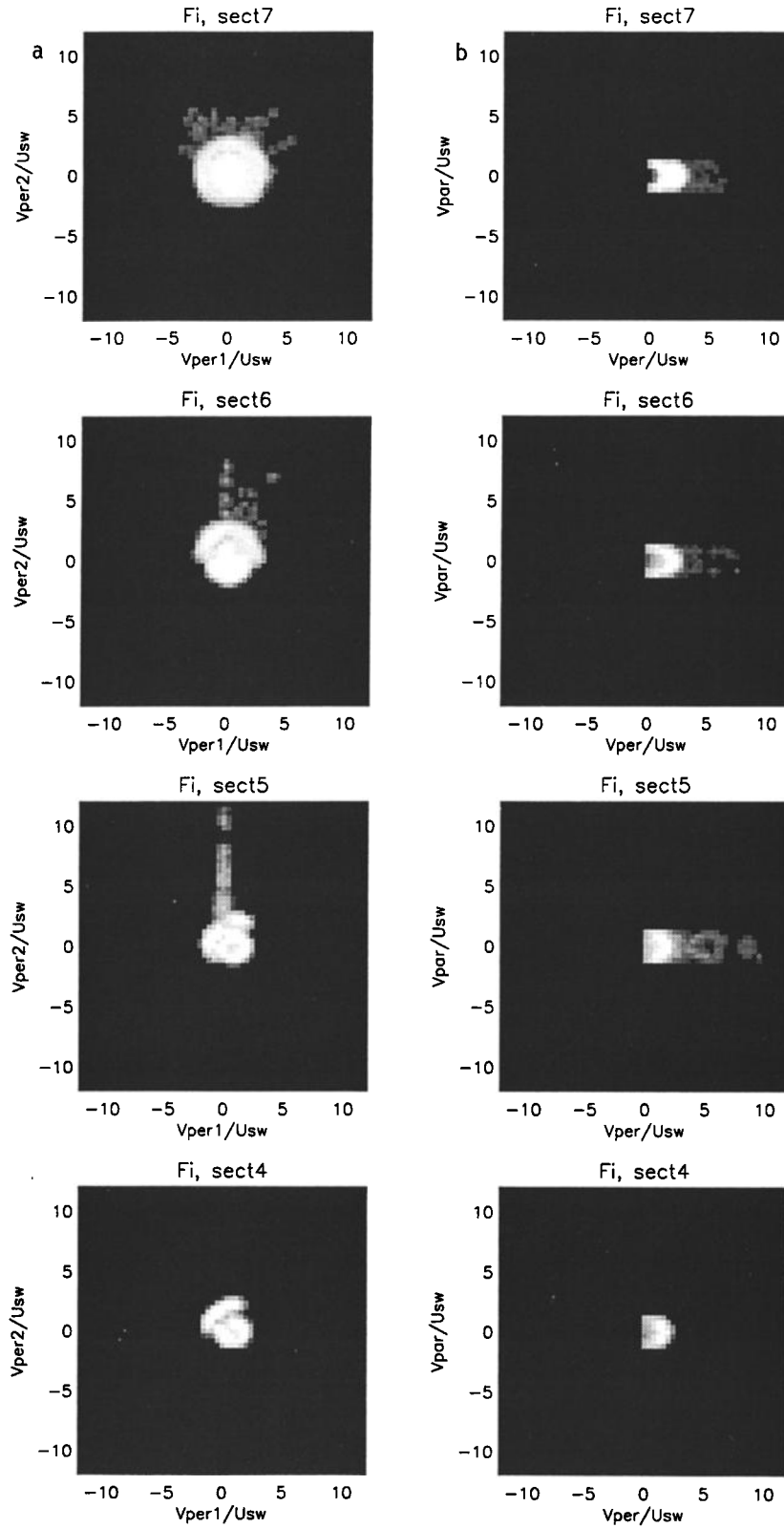


Figure 11. The projection of the PI distribution onto the velocity plane for downstream and upstream sections when a power law turbulent spectrum $P(K) \propto K^\alpha$ is assumed. Here v_\perp and v_\parallel are the velocity components perpendicular to and parallel to the magnetic field, respectively.

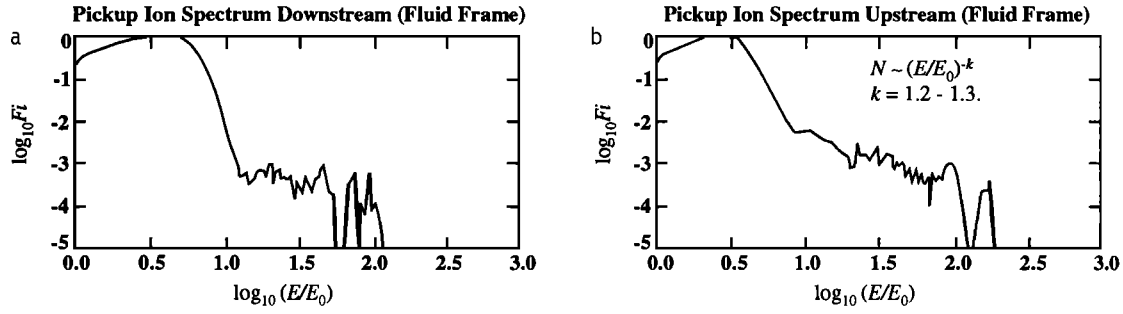


Figure 12. The energy spectrum of accelerated He^+ PIs (a) downstream of a perpendicular shock and (b) upstream of a perpendicular shock.

of accelerated PIs on the ramp thickness. The simulation demonstrates a reasonable qualitative agreement with the analytical estimate. It is clear from Figure 13 that hybrid or particle simulations which exhibit a broad shock ramp cannot simulate the MRI acceleration mechanism. This may place strong constraints on, for example, the strength of the numerical dissipation used in hybrid or particle codes were one to use this approach to investigate self-consistently MRI acceleration. It is also important to use a very small time step ($\Delta t \ll \Delta z/v$) in order to calculate accurately the trajectory of a PI in the vicinity of the ramp. For MRI acceleration of H^+ and He^+ ions to be viable, a ramp thickness comparable to the electron inertial length is needed, whereas for heavy ions it is sufficient for the ramp to have a thickness comparable to the ion inertial length.

4. Conclusions

Particle-mesh simulations of the acceleration of pickup ions at collisionless quasi-perpendicular shocks with an assumed fixed profile for the transition layer have demonstrated several new features, as well as providing support for the basic analysis of Zank *et al.* [1996b] and Lee *et al.* [1996]. Our results may be enumerated as follows.

1. The energy spectrum of accelerated H^+ PIs at quasi-perpendicular shocks may be approximated by the power law $F_i(E) \approx (E/E_0)^{-k}$, where k varies from 0.92 to 1.2. This spectrum is a little harder than that obtained by the quasi-analytical approach of Zank *et al.*, but both approaches give spectra which are considerably harder than those predicted by diffusive shock acceleration. The accelerated ion spectra are found to flatten as θ_{bn} decreases from 90° until particle escape upstream ensures that PIs no longer return to the shock and MRI acceleration effectively ceases.

2. The fine structure of the shock may slightly decrease the maximum energy of accelerated pickup ions compared to that of a step-like transition layer.

3. A flat turbulence spectrum in the shock transition layer results in an increased maximum PI energy for particles downstream of the shock, whereas power law turbulence reduces the maximum PI energy gain. The basic mechanism of MRI acceleration is, however, preserved, and hard spectra result.

4. The energy spectrum of accelerated He^+ PIs at quasi-perpendicular shocks may also be approximated by the power law $F_i(E) \approx (E/E_0)^{-k}$, where k varies between 1.2 and 1.3. As expected, the injection efficiency of pickup He^+ is substantially less than that of pickup H^+ .

5. For oblique shocks with $\theta_{bn} = 60^\circ$ to $\theta_{bn} \approx 70^\circ$ a strong beam of PIs is formed along the magnetic field. In a self-consistent simulation the reflected PI beam might be expected to drive further low-frequency plasma instabilities.

6. Hybrid or particle codes, which effectively resolve the shock ramp numerically (with $L_{\text{ramp}} \gg 0.01 r_{ci}$ and $\Delta t \gg 10^{-4} T_{ci}$, where $r_{ci} = M_A c / \omega_{pi}$ is the ion gyroradius and T_{ci} the ion gyroperiod) are inadequate for investigating MRI acceleration. For MRI acceleration of H^+ and He^+ ions to be effective, a ramp thickness comparable to the electron inertial length scale is needed, whereas for heavy ions it is sufficient to have a ramp thickness comparable to that of the ion inertial length.

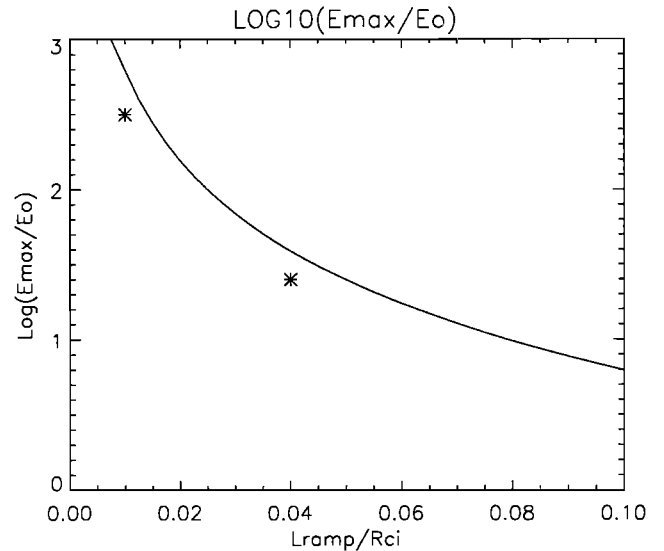


Figure 13. The dependence of the maximum energy of accelerated PIs on the ramp thickness. Here an asterisk denotes the results from the particle-mesh simulation, and the solid line corresponds to the estimate by Zank *et al.* [1996b]: $\log_{10}(E_{\text{max}}/E_0) = 2\log_{10}(\eta(r-1)/M_A^2) - 2\log_{10}(L_{\text{ramp}}/r_{ci})$.

Thus the key factor determining the efficacy of MRI acceleration is the existence of a strong steep ramp inside the shock transition layer. Whether such a ramp exists is, at present, unclear, both observationally and theoretically. Furthermore, under more realistic circumstances the ramp structure in a quasi-perpendicular shock, even with a large θ_{bn} ($\theta_{bn} \approx 80^\circ - 90^\circ$), may be nonstationary, experiencing cyclical changes which are characterized by a progressive steepening and smoothing of the electromagnetic field in the shock transition layer. This behavior may result in the appearance of sporadic bursts of accelerated PIs at the shock front. Clearly, the next step in this investigation is to consider self-consistent simulations in which the fine structure of the shock wave is very carefully resolved.

Acknowledgments. G.P.Z., H.L.P., and A.S.L. were supported in part by an NSF-DOE grant ATM 9713223, NASA grant NAG5-6469, and an NSF Young Investigator Award ATM-9357861. Partial support by JPL contract 959167 and a NASA Delaware Space grant NGT5-40024 is hereby acknowledged. Computational resources were provided by the Computer Center, University of Delaware (Cray-J90), and by the NSF San Diego Supercomputer Center (Cray-C90). A.S.L. and G.P.Z. thank the referees for their fruitful comments.

The Editor thanks the referees for their assistance in evaluating this paper.

References

- Armstrong, T.P., M.E. Pesses, and R.B. Decker, Shock drift acceleration, in *Collisionless Shocks in the Heliosphere: Reviews of Current Research*, *Geophys. Monogr. Ser.*, vol. 35, edited by B.T. Tsurutani and R.G. Stone, p. 271, AGU, Washington, D.C., 1985.
- Balikhin, M., V. Krasnoselskikh and M. Gedalin, The scales in quasi-perpendicular shocks, in *Physics of Collisionless Shocks*, edited by C.T. Russell, *Adv. Space Res.*, 15, p. 247, 1995.
- Decker, R.B., Formation of shock-spike events at quasiperpendicular shocks, *J. Geophys. Res.*, 88, 9959, 1983.
- Decker, R.B., Computer modeling of test particle acceleration at oblique shocks, *Space Sci. Rev.*, 48, 195, 1988.
- Decker, R.B., and L. Vlahos, Numerical studies of particle acceleration of turbulent, oblique shocks with an application to prompt ion acceleration during solar flares, *Astrophys. J.*, 306, 710, 1986.
- Forslund, D.W., K.B. Quest, J.U. Brackbill, and K. Lee, Collisionless dissipation in quasi-perpendicular shocks, *J. Geophys. Res.*, 89, 2142, 1984.
- Galeev, A.A., and A.S. Lipatov, Plasma processes in cometary atmospheres, *Adv. Space Res.*, 4, (9), 229, 1984.
- Galeev, A.A., A.S. Lipatov, and R.Z. Sagdeev, Numerical simulation of shock waves near comets: Structural features and energy dissipation mechanisms, *Sov. Phys. JETP, Engl. Transl.*, 62, (5), 866, 1985.
- Galeev, A.A., A.S. Lipatov, and R.Z. Sagdeev, Two-dimensional numerical simulation of the relaxation of cometary ions and MHD turbulence in the flow of the solar wind around a cometary atmosphere, *Sov. J. Plasma Phys., Engl. Transl.*, 13, (5), 323, 1987.
- Galeev, A.A., A.S. Lipatov, and A.A. Malgichev, Numerical simulation of the structure of an oblique collisionless shock wave including electron inertia, *Sov. J. Plasma Phys.*, 17, (10), 701, 1991.
- Giachalone, J., J.R. Jokipii, and J. Kóta, Ion injection and acceleration at quasi-perpendicular shocks, *J. Geophys. Res.*, 99, 19,351, 1994.
- Gloeckler, G., J. Geiss, E.C. Roelof, L.A. Fisk, F.M. Ipavich, K.W. Ogilvie, L.J. Lanzerotti, R. von Steiger, and B. Wilken, Acceleration of interstellar pickup ions in the disturbed solar wind observed on Ulysses, *J. Geophys. Res.*, 99, 17,637, 1994.
- Goodrich, C.C., Numerical simulations of quasi-perpendicular collisionless shocks, in *Collisionless Shocks in the Heliosphere: Reviews of Current Research*, *Geophys. Monogr. Ser.*, vol. 35, edited by B.T. Tsurutani and R.G. Stone, p. 153, AGU, Washington, D.C., 1985.
- Jokipii, J.R., J. Kóta, and J. Giacalone, Perpendicular transport in 1- and 2-dimensional shock simulation, *Geophys. Res. Lett.*, 20, 1759, 1993.
- Katsouleas, T., and J.M. Dawson, Unlimited electron acceleration in laser-driven plasma waves, *Phys. Rev. Lett.*, 51, 392, 1983.
- Kennel, C.F., J.P. Edmiston, and T. Hada, A quarter century of collisionless shock research, in *Collisionless Shocks in the Heliosphere: A Tutorial Review*, *Geophys. Monogr. Ser.*, vol. 34, edited by R.G. Stone and B.T. Tsurutani, pp. 1-36, AGU, Washington, D.C., 1985.
- Kucharek, H., and M. Scholer, Injection and acceleration of interstellar pickup ions at the heliospheric termination shock, *J. Geophys. Res.*, 100, 1745, 1995.
- Lee, M.A., V.D. Shapiro, and R.Z. Sagdeev, Pickup ion energization by shock surfing, *J. Geophys. Res.*, 101, 4777, 1996.
- Lembege, B., and J.M. Dawson, Formation of double layers within an oblique collisionless shock, *Phys. Rev. Lett.*, 62, 2683, 1989.
- Leroy, M.M., Structure of perpendicular shocks in collisionless plasma, *Phys. Fluids*, 26, 2742, 1983.
- Leroy, M.M., D. Winske, C.C. Goodrich, C.S. Wu, and K. Papadopoulos, The structure of Perpendicular Bow Shocks, *J. Geophys. Res.*, 87, 5081, 1982.
- Liewer, P.C., B.E. Goldstein, and N. Omid, Hybrid simulations of the effects of interstellar pickup hydrogen on the solar wind termination shock, *J. Geophys. Res.*, 98, 15,211, 1993.
- Liewer, P.C., S. Rath, and B.E. Goldstein, Hybrid simulations of the interstellar pickup ion acceleration at the solar wind termination shock, *J. Geophys. Res.*, 100, 19,809, 1995.
- Lipatov, A.S., Numerical simulation of the one-dimensional structure of a quasiperpendicular collisionless shock, *Cosmic Res. Engl. Transl.*, 32, (1), 72, 1994.
- Lipatov, A.S., 3D and 2.5D hybrid multiscale simulation technology: Application to study of forced nonstationary processes at tangential discontinuities, *Int. STEP News.*, 5, (16), 11, 1996.
- Lipatov, A.S., and V.A. Lobatchev, Numerical kinetic simulation of the One-dimensional structure of oblique and quasi-perpendicular collisionless shocks, *Cosmic Res. Engl. Transl.*, 34, (5), 420, 1996.
- Lipatov, A.S., and I.N. Syrovatskii, Numerical modeling of circumcometary quasiparallel shocks, *Cosmic Res. Engl. Transl.*, 25, (6), 750, 1987.
- Newbury, J.A., and C.T. Russell, Observations of a very thin collisionless shock (abstract), *EOS Trans. AGU*, 75, (44) Fall Meet. Suppl., 533, 1994.
- Omid, N., and D. Winske, A kinetic study of solar wind mass loading and cometary bow shocks, *J. Geophys. Res.*, 92, 13,409, 1987.
- Quest, K.B., Simulations of high Mach number collisionless perpendicular shocks in astrophysical plasmas, *Phys. Rev. Lett.*, 54, 1872, 1985.
- Quest, K.B., Simulation of high Mach number perpendicular

- lar shocks with resistive electrons, *J. Geophys. Res.*, **91**, 8805, 1986.
- Sagdeev, R.Z., Cooperative phenomena and shock waves in collisionless plasmas, in *Reviews of Plasma Physics*, vol. 4, edited by M.A. Leontovich, p. 23, Consult. Bur., New York, 1966.
- Sagdeev, R.Z., and V.D. Shapiro, Influence of transverse magnetic field on Landau Damping, *JETP Lett. Engl. Transl.*, **17**, 279, 1973.
- Sagdeev, R.Z., V.D. Shapiro, V.I. Shevchenko, and K. Szego, MHD turbulence in the solar wind-comet interaction region, *Geophys. Res. Lett.*, **13**, 85, 1986.
- Sckopke, N., Ion heating at the Earth's quasi-perpendicular bow shock, *Adv. Space Res.*, **15**(8/9), 261, 1995.
- Scudder, J.D., A. Mangeney, C. Lacombe, C.C. Harvey, T.L. Aggson, R.R. Anderson, J.T. Gosling, G. Paschmann, and C.T. Russell, The resolved layer of a collisionless, high β , supercritical, quasi-perpendicular shock wave, 1, Rankine-Hugoniot geometry, currents, and stationarity, *J. Geophys. Res.*, **91**, 11,019, 1986.
- Tokar, R.L., C.H. Aldrich, D.W. Forslund, and K.B. Quest, Nonadiabatic electron heating at high Mach number perpendicular shocks, *Phys. Rev. Lett.*, **56**, 1909, 1986.
- Vasyliunas, V.M., and G.L. Siscoe, On the flux and the energy spectrum of interstellar ions in the solar system, *J. Geophys. Res.*, **81**, 1247, 1976.
- Winske, D., Microtheory of collisionless shock current layers, in *Collisionless Shocks in the Heliosphere: Reviews of Current Research*, *Geophys. Monogr. Ser.*, vol. 35, edited by B.T. Tsurutani and R.G. Stone, p. 225, AGU, Washington, D.C., 1985.
- Winske, D., and P.S. Gary, Electromagnetic instabilities driven by cool heavy ion beam, *J. Geophys. Res.*, **91**, 6825, 1986.
- Winske, D., C.S. Wu, Y.Y. Li, Z.Z. Mou, and Y.S.Y. Guo, Coupling of newborn ions to the solar wind by electromagnetic instabilities and their interaction with the bow shock, *J. Geophys. Res.*, **90**, 2713, 1985.
- Wu, C.S., and R.C. Davidson, Electromagnetic instabilities produced by neutral-particle ionization in interplanetary space, *J. Geophys. Res.*, **77**, 5399, 1972.
- Wu, C.S., D. Winske, and J.D. Gaffey Jr., Rapid pick-up of cometary ions due to strong magnetic turbulence, *Geophys. Res. Lett.*, **13**, 865, 1986.
- Zank, G.P., I.H. Cairns, and G.M. Webb, The termination shock: Physical processes, *Adv. Space Res.*, **15**(8/9), 453, 1995.
- Zank, G.P., W.H. Matthaeus, and C.W. Smith, Evolution of turbulent magnetic fluctuation power with heliospheric distance, *J. Geophys. Res.*, **101**, 17,093, 1996a.
- Zank, G.P., H.L. Pauls, I.H. Cairns, and G.M. Webb, Interplanetary pickup ions and quasi-perpendicular shocks: Implications for the termination shock and interplanetary shocks, *J. Geophys. Res.*, **101**, 457, 1996b.
- Zilbersher, D., and M. Gedalin, Pickup ion dynamics at the structured quasi-perpendicular shock, *Planet. Space Sci.*, **45**(6), 693, 1997.

A. S. Lipatov, Dialogue-Science Inc., Computer Center, Russian Academy of Sciences, Moscow, 117333 Russia.

H. L. Pauls and G. P. Zank, Bartol Research Institute, University of Delaware, Newark, DE 19716-4793. (e-mail: zank@bartol.udel.edu)

(Received October 20, 1997; revised August 12, 1998; accepted August 13, 1998.)